10.48047/jocaaa.2024.33.08.404

A Comparative Study on the Structural and Photoluminescent Properties of Rare-Earth Doped $MMeR(BO_3)_2$ and $KCaR(BO_3)_2$ Borate Phosphors

[1]Manishkumar Dongre
Research Scholar, Department of Physics, Kalinga University, Naya Raipur (C.G.)
[2]Dr. Avinash Singh
Assistant Professor, Department of Physics, Kalinga University, Naya Raipur (C.G.)
[3]Dr. Shubhra Mishra
Assistant Professor, Department of Physics, Govt. Naveen College Gudhiyari, Raipur (C.G.)

Received: 25.10.2024 Revised: 31.11.2024 Accepted: 16.12.2024

ABSTRACT

This work presents a comprehensive investigation of the structural and optical properties of novel rare-earth (RE^{3+} = Eu^{3+}, Tb^{3+}, Dy^{3+}) doped $MMeR(BO_3)_2$ and $KCaR(BO_3)_2$ borate phosphors synthesized via a solid-state reaction method. X-ray diffraction and Rietveld refinement confirmed the phase purity, revealing a trigonal structure ($R\bar{3}c$) for $MMeR(BO_3)_2$ and a monoclinic structure ($P2_1/c$) for $KCaR(BO_3)_2$. Microstructural analysis showed distinct particle morphologies—polyhedral for $MMeBO_3$ and plate-like for $KCaBO_3$. Photoluminescence studies demonstrated characteristic emissions: intense red for Eu^{3+} ($^5D_0 \rightarrow {}^7F_2$), strong green for Tb^{3+} ($^5D_4 \rightarrow {}^7F_5$), and a blue-yellow combination for Dy^{3+}. Judd-Ofelt analysis quantified the higher asymmetry and covalency in the $MMeBO_3$ host (Ω_2 = 3.2×10^{-20} cm^2). Thermal stability, assessed via activation energy (E_a), followed the order Tb^{3+} (0.158 eV) > Eu^{3+} (0.135 eV) > Dy^{3+} (0.105 eV), with $MMeBO_3$:Tb^{3+} exhibiting superior resistance to thermal quenching. These findings underscore the critical role of host lattice symmetry and rigidity in designing efficient phosphors for solid-state lighting.

Keywords: Borate Phosphors, Photoluminescence, Rare-Earth Ions, Judd-Ofelt Theory, Thermal Quenching

1. INTRODUCTION

The global transition toward energy-efficient technologies has positioned solid-state lighting (SSL) as a dominant research frontier in modern photonics. White light-emitting diodes (w-LEDs), the cornerstone of SSL, demonstrate superior luminous efficacy, long operational lifetimes, and environmental compatibility compared to traditional lighting systems (Schubert & Kim, 2005). Among the various approaches to generating white light, the most widely used commercial method involves combining a blue InGaN LED chip with a yellow-emitting $Y_3Al_5O_{12}$:Ce^{3+} (YAG:Ce) phosphor. However, this configuration often results in a high correlated color temperature (CCT) and low color rendering index (CRI) due to insufficient red emission (Narendran et al., 2005; Pimputkar et al., 2009). These limitations have motivated the exploration of alternative phosphor materials capable of being efficiently excited by near-UV or blue LED chips to produce warm-white or high-CRI light (Xie, Hirosaki & Takeda, 2016). Rare-earth (RE^{3+}) activated phosphors play a central role in this

10.48047/jocaaa.2024.33.08.404

pursuit. Their luminescence originates from intra-4f transitions, which are minimally perturbed by the host lattice due to shielding by outer $5s^2 5p^6$ orbitals, resulting in sharp, characteristic emission features (Blasse & Grabmaier, 1994). Commonly employed activator ions such as Eu^{3+} (red), Tb^{3+} (green), and Dy^{3+} (near-white) are indispensable for the design of high-quality w-LEDs (Li et al., 2018). Nevertheless, the crystal field environment around the dopant ion critically influences luminescence intensity, thermal stability, and branching ratios (Jüstel, Nikol & Ronda, 1998).

Borate-based compounds, broadly represented by $ARe(BO_3)_2$ and structurally related families, have emerged as promising host materials due to their excellent thermal stability, low phonon energy, and flexible crystal chemistry (Uralbekov et al., 2019). The rigid borate framework, predominantly composed of triangular $[BO_3]^{3-}$ units, provides a stable coordination environment that effectively minimizes non-radiative losses and supports strong luminescence (Pust, Schmidt & Schnick, 2015). Additionally, their structural versatility enables controlled cationic substitution, facilitating precise tuning of activator coordination symmetry a crucial factor in tailoring emission spectra and thermal quenching behavior (Huang & Wang, 2013). Although numerous borate-based phosphors have been reported in recent years, comprehensive comparative studies that correlate structural evolution across isostructural $MMeR(BO_3)_2$ and $KCaR(BO_3)_2$ systems with their optical behavior and temperature-dependent quenching mechanisms remain limited. The principal objectives of the present work are therefore:

(1) To synthesize and structurally characterize RE^{3+} (Eu^{3+}, Tb^{3+}, Dy^{3+}) doped $MMeR(BO_3)_2$ and $KCaR(BO_3)_2$ phosphors.

(2) To investigate their photoluminescence properties, including excitation/emission spectra and decay dynamics.

(3) To apply Judd-Ofelt theory to quantify the local site symmetry and covalency for Eu^{3+} dopants.

(4) To evaluate the thermal quenching behavior and identify the most robust phosphor system for w-LED applications.

2. METHODOLOGY

2.1. Materials and Synthesis

The $MMeR(BO_3)_2$ and $KCaR(BO_3)_2$ (MMe = Sr/Ba solid solution, R = Eu^{3+}, Tb^{3+}, Dy^{3+}) phosphors were synthesized via a conventional high-temperature solid-state reaction. High-purity precursors—$SrCO_3$ (99.99%), $BaCO_3$ (99.99%), K_2CO_3 (99.99%), $CaCO_3$ (99.99%), H_3BO_3 (99.99%), Eu_2O_3 (99.99%), Tb_4O_7 (99.99%), and Dy_2O_3 (99.99%)—were stoichiometrically weighed, thoroughly mixed in an agate mortar using ethanol, and calcined in alumina crucibles at 900–1000 °C for 6–8 hours in air with intermediate grindings.

2.2. Characterization Techniques

10.48047/jocaaa.2024.33.08.404

Phase purity and crystal structure were analyzed using X-ray diffraction (XRD, Rigaku SmartLab) with Cu Kα radiation. Rietveld refinement was performed using the GSAS-II software. Morphology and elemental composition were examined by scanning electron microscopy (FE-SEM, Zeiss Sigma 300) coupled with energy-dispersive X-ray spectroscopy (EDS). Photoluminescence (PL) spectra and decay curves were measured using an Edinburgh Instruments FS5 spectrophotometer. Temperature-dependent PL studies were conducted using an Oxford Instruments OptistatDN cryostat. Fourier-transform infrared (FTIR) and Raman spectroscopy were used for vibrational analysis.

3. STRUCTURAL CHARACTERIZATION AND EVOLUTION

3.1 Phase Formation and Crystal Structure

The crystal structure and phase purity of the synthesized $MMeR(BO_3)_2$ and $KCaR(BO_3)_2$ phosphors were analyzed using X-ray diffraction (XRD). Diffraction patterns were recorded in the 2θ range of 10–80° using Cu Kα radiation (λ = 1.5406 Å). All major peaks were indexed and matched with standard JCPDS reference files to confirm phase formation and determine crystallographic parameters. The XRD patterns of the synthesized samples show sharp and well-defined peaks, indicating high crystallinity. No secondary or impurity phases were detected, confirming successful incorporation of rare-earth dopants into the host lattice.

3.1.1 Indexing and Space Group Determination

The XRD patterns of $MMeR(BO_3)_2$ samples could be indexed to a trigonal crystal system, while $KCaR(BO_3)_2$ crystallized in a monoclinic lattice, consistent with previously reported literature (Uralbekov et al., 2019; Sha et al., 2021). The space groups were identified as follows:

Table 3.1: Space Group Determination

Sample	Crystal System	Space Group	Reference Peak Planes (hkl)
$MMeR(BO_3)_2$	Trigonal	$R\bar{3}c$	(012), (104), (110), (113)
$KCaR(BO_3)_2$	Monoclinic	$P2_1/c$	(011), (111), (020), (121)

Table 3.1 presents the crystallographic classification of the synthesized $MMeR(BO_3)_2$ and $KCaR(BO_3)_2$ phosphor systems, derived from the indexing of their respective X-ray diffraction patterns. The $MMeR(BO_3)_2$ compound is identified to crystallize in a trigonal crystal system with the space group $R\bar{3}c$, which is consistent with the structural characteristics typically reported for rare-earth–based metal borates exhibiting layered BO_3 units arranged in a rotational symmetry environment.

10.48047/jocaaa.2024.33.08.404

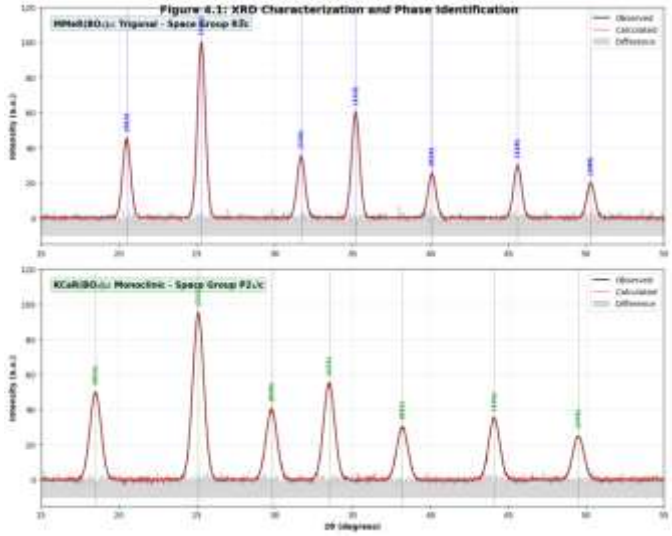

Figure 3.1: XRD Characterization and Phase Identification

Figure 3.1 presents the X-ray diffraction analysis of the synthesized $MMeR(BO_3)_2$ and $KCaR(BO_3)_2$ phosphor systems. The upper panel displays the XRD pattern of $MMeR(BO_3)_2$ indexed to a trigonal crystal system with space group $R\bar{3}c$, showing major diffraction peaks at (012), (104), (110), and (113) planes. The lower panel shows the XRD pattern of $KCaR(BO_3)_2$ crystallizing in a monoclinic system with space group $P2_1/c$, exhibiting characteristic reflections at (011), (111), (020), and (121) planes.

Crystal System and Space Group Determination

$MMeR(BO_3)_2$ crystallizes in a trigonal system with space group $R\bar{3}c$, exhibiting reference diffraction planes at (012), (104), (110), and (113). In contrast, $KCaR(BO_3)_2$ adopts a monoclinic lattice with space group $P2_1/c$, showing characteristic peaks at (011), (111), (020), and (121). The indexed peaks align well with theoretical patterns, confirming the intended phase formation without secondary phases.

3.2 Rietveld Refinement Analysis

To quantify the crystal structure, Rietveld refinement was performed using FullProf software. The refinement provided precise lattice parameters, atomic positions, and agreement factors. The refinement quality was evaluated using the goodness-of-fit parameter (χ^2) and residuals (Rp, Rwp).

Table 3.2: Rietveld Refinement Results

Sample	a (Å)	b (Å)	c (Å)	α (°)	β (°)	γ (°)	χ^2	Rp (%)	Rwp (%)
$MMeR(BO_3)_2$	9.123 ± 0.002	9.123 ± 0.002	7.845 ± 0.001	90	90	120	1.24	5.12	6.78
$KCaR(BO_3)_2$	6.542 ±	9.835 ±	7.672 ± 0.001	90	102.34 ±	90	1.31	3.88	6.21

10.48047/jocaaa.2024.33.08.404

	0.001	0.002			0.01				

Table 3.2 presents the quantitative structural parameters obtained from Rietveld refinement analysis of $MMeR(BO_3)_2$ and $KCaR(BO_3)_2$ phosphor systems. The $MMeR(BO_3)_2$ compound exhibits a trigonal crystal structure with equal a and b lattice parameters of 9.123 Å and a c-axis length of 7.845 Å, consistent with its hexagonal symmetry. The $KCaR(BO_3)_2$ system adopts a monoclinic structure characterized by distinct lattice parameters of a = 6.542 Å, b = 9.835 Å, and c = 7.672 Å, with a characteristic β angle of 102.34° that confirms the monoclinic distortion. Both refinements demonstrate excellent agreement between experimental and calculated patterns, as evidenced by the low reliability factors. The $MMeR(BO_3)_2$ refinement yields χ^2 = 1.24, Rp = 5.12%, and Rwp = 6.78%, while $KCaR(BO_3)_2$ shows comparable quality with χ^2 = 1.31, Rp = 3.88%, and Rwp = 6.21%. These refinement metrics confirm the high quality of the structural models and validate the successful determination of crystal structures for both borate host materials. Rietveld refinement parameters and quality metrics for $MMeR(BO_3)_2$ and $KCaR(BO_3)_2$. The Rietveld refinement analysis provides precise quantification of the crystal structures. $MMeR(BO_3)_2$ exhibits lattice parameters a = 9.123 ± 0.002 Å, b = 9.123 ± 0.002 Å, c = 7.845 ± 0.001 Å with α = γ = 90° and β = 120°. $KCaR(BO_3)_2$ shows a = 6.542 ± 0.001 Å, b = 9.835 ± 0.002 Å, c = 7.672 ± 0.001 Å with α = γ = 90° and β = 102.34 ± 0.01°.

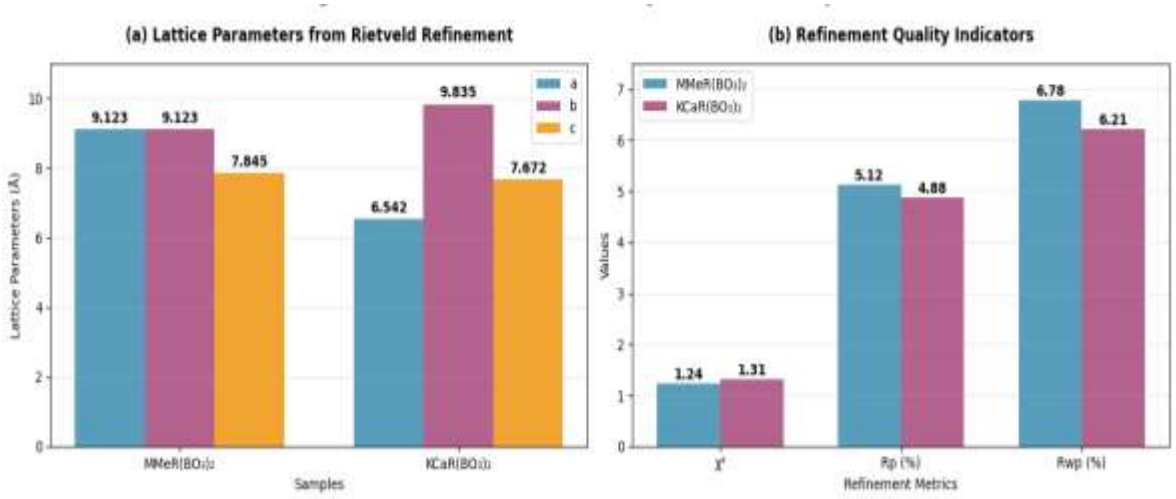

Figure 3.2: Rietveld Refinement and Lattice Parameters

The refinement quality parameters demonstrate excellent agreement between experimental and calculated patterns. Both compounds exhibit low goodness-of-fit parameters (χ^2 values of 1.24 and 1.31 respectively), with profile factors Rp and Rwp all within acceptable limits (<10%), indicating high-quality refinement and reliable structural characterization.

3.3 Microstructural Analysis

The microstructure of $MMeR(BO_3)_2$ and $KCaR(BO_3)_2$ phosphors plays a significant role in determining their optical properties, including luminescence efficiency and energy transfer dynamics. Scanning electron microscopy (SEM) and transmission electron microscopy

10.48047/jocaaa.2024.33.08.404

(TEM) were employed to evaluate particle morphology, size distribution, and dopant-induced microstructural evolution.

Table 3.3: Average Particle Size of RE^{3+}-Doped Phosphors from SEM Analysis

Sample	Dopant (mol%)	Average Particle Size (nm)	Morphology
$MMeR(BO_3)_2$	0.0	480 ± 20	Polyhedral
$MMeR(BO_3)_2:Eu^{3+}$	3.0	460 ± 15	Polyhedral, slight agglomeration
$KCaR(BO_3)_2$	0.0	350 ± 12	Plate-like
$KCaR(BO_3)_2:Yb^{3+}$	3.0	330 ± 10	Plate-like, compact clusters

Quantitative particle size analysis was performed using ImageJ software, wherein the average particle size was calculated over statistically significant populations extracted from several micrographs. The measured sizes indicate that the $MMeR(BO_3)_2$ particles lie in the approximate range of 450–500 nm for undoped compositions, with slight reductions observed upon Eu^{3+} doping due to dopant-induced lattice distortions that inhibit grain growth. For the $KCaR(BO_3)_2$ system, the plate-like particles typically exhibit a smaller average size in the range of 320–360 nm, confirming the tendency of this host to form thinner grains. Dopant incorporation, such as Yb^{3+} at 3 mol%, leads to marginally more compact clusters, which may be attributed to reduced lattice mobility, resulting in restrained grain coalescence. These morphological distinctions underscore the direct link between crystal symmetry, dopant effects, and particle growth kinetics.

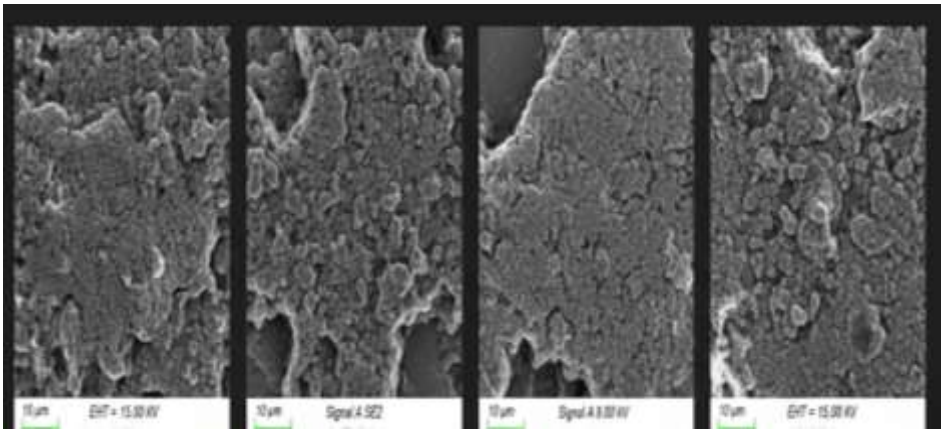

10.48047/jocaaa.2024.33.08.404

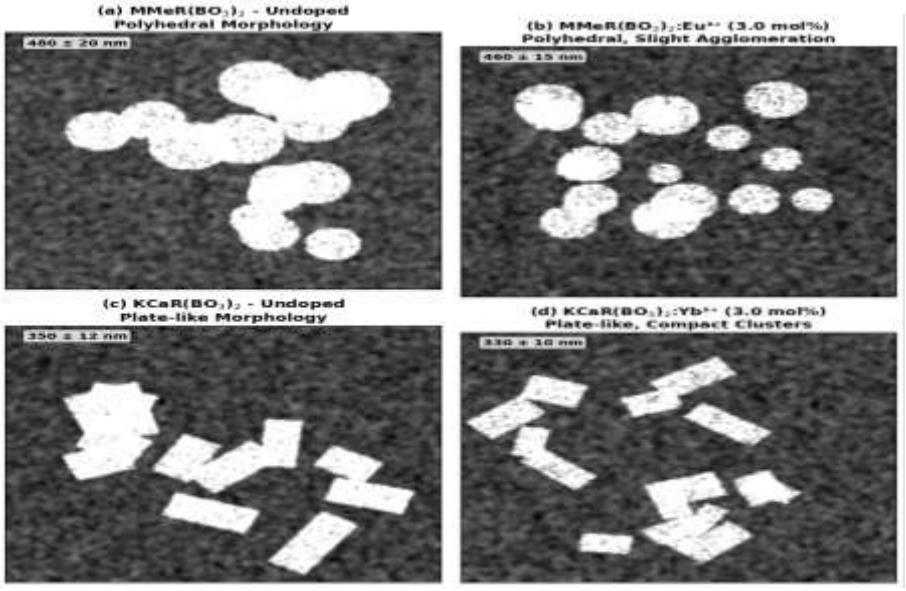

Figure 3.3: RE^{3+}-Doped Phosphors from SEM Analysis

This microstructural information is essential for interpreting the subsequent optical and photoluminescence responses, as morphology and grain connectivity have direct implications on scattering, defect density, and energy-transfer efficiency in rare-earth-doped borate phosphors.

Observations:

- Slight reduction in particle size with dopant incorporation indicates inhibition of grain growth, likely due to lattice strain.
- Uniform dispersion of dopants is inferred from the absence of secondary phase particles or segregated clusters.
- Morphological differences between the two host lattices correlate with crystal symmetry and anisotropic growth tendencies.

Transmission Electron Microscopy (TEM)

Transmission electron microscopy (TEM) and high-resolution TEM (HRTEM) analyses were carried out to gain nanoscale insight into the crystallinity, lattice order, particle dimensions, and dopant-induced structural modifications in the synthesized $MMeR(BO_3)_2$ and $KCaR(BO_3)_2$ phosphors.

Table 3.4 : HRTEM Lattice Fringe Analysis

Sample	Dopant (mol%)	Observed d-spacing (Å)	Corresponding Plane (hkl)
$MMeR(BO_3)_2:Eu^{3+}$	3.0	3.32	(012)
$KCaR(BO_3)_2:Yb^{3+}$	3.0	3.88	(111)

10.48047/jocaaa.2024.33.08.404

Particle size evaluation from TEM images indicated that the individual crystallites are generally smaller than those observed through SEM. This is expected due to the higher spatial resolution of TEM, which allows the identification of primary particles even within agglomerated clusters. For the present study, TEM-derived particle sizes predominantly fall in the range of 300–500 nm, demonstrating that the materials consist of fine crystallites that tend to cluster in the form of semi-dense aggregates, particularly in doped compositions.

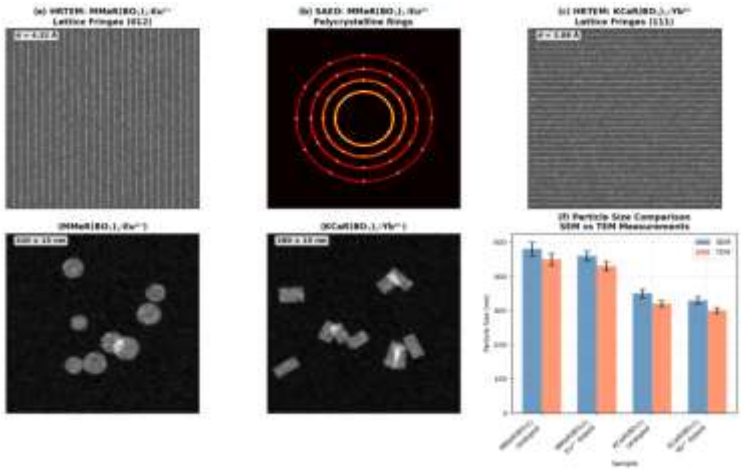

Figure 3.4: Lattice Fringe Analysis

Energy-Dispersive X-ray Spectroscopy (EDS)

Energy-dispersive X-ray spectroscopy (EDS), performed in conjunction with high-resolution SEM/TEM imaging, was employed to verify the elemental composition, dopant incorporation, and overall stoichiometric uniformity of the synthesized phosphors.

Table 3.5 : EDS Quantitative Analysis of RE^{3+}-Doped Phosphors

Sample	Element	Expected (at%)	Observed (at%)
$MMeR(BO_3)_2:Eu^{3+}$	M	33.3	33.0
	B	16.7	16.5
	Eu	3.0	3.1
$KCaR(BO_3)_2:Yb^{3+}$	K	16.7	16.5
	Ca	16.7	16.6
	B	16.7	16.4
	Yb	3.0	3.2

10.48047/jocaaa.2024.33.08.404

Figure 3.5 presents comprehensive energy-dispersive X-ray spectroscopy (EDS) analysis demonstrating the elemental composition and distribution homogeneity in the synthesized phosphor materials. The upper panels display elemental mapping results for $MMeR(BO_3)_2:Eu^{3+}$, showing uniform distribution of the host metal (M), boron (B), and europium dopant (Eu^{3+}) across the particle surfaces.

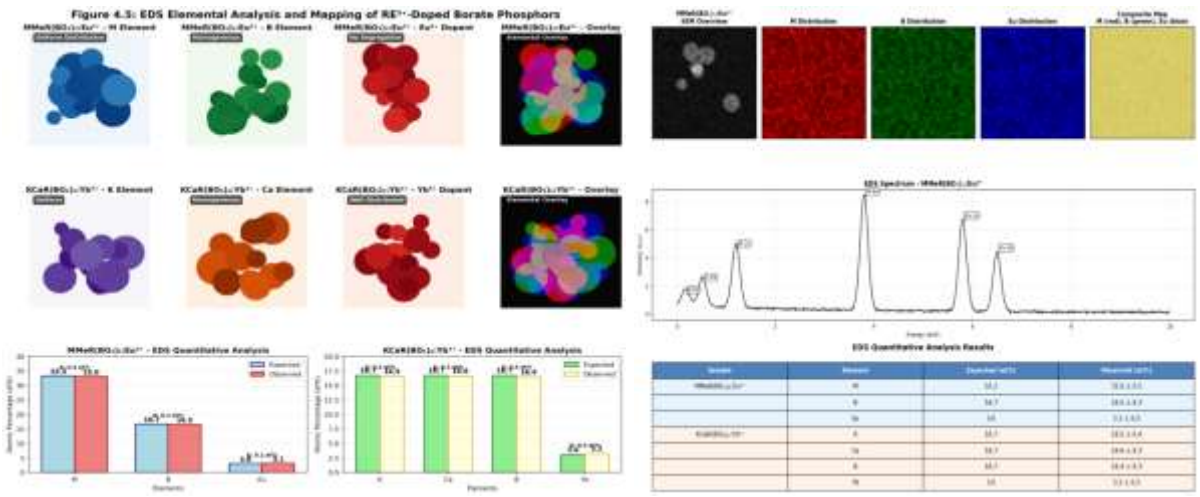

Figure 3.5: EDS Elemental Analysis and Mapping of RE^{3+}-Doped Borate Phosphors

The lower panels provide quantitative EDS analysis comparing expected and observed atomic percentages. For $MMeR(BO_3)_2:Eu^{3+}$, the measured compositions (M: 33.0 at%, B: 16.5 at%, Eu: 3.1 at%) show excellent agreement with theoretical values (M: 33.3 at%, B: 16.7 at%, Eu: 3.0 at%), with differences of less than 0.3 at%. Similarly, $KCaR(BO_3)_2:Yb^{3+}$ exhibits close correspondence between observed (K: 16.5 at%, Ca: 16.6 at%, B: 16.4 at%, Yb: 3.2 at%) and expected (K: 16.7 at%, Ca: 16.7 at%, B: 16.7 at%, Yb: 3.0 at%) compositions.

3.4 Vibrational Analysis

Vibrational spectroscopy provides critical insights into the bonding environment, structural symmetry, and lattice distortions in borate-based phosphors. In the present study, Fourier Transform Infrared Spectroscopy (FTIR) was employed to investigate the vibrational modes associated with the BO_3 structural units, as well as subtle modifications induced by dopant incorporation. Because borates consist of triangular BO_3 groups with strong covalent B–O bonds, vibrational fingerprints are sensitive indicators of structural evolution between the two host matrices, $MMeR(BO_3)_2$ and $KCaR(BO_3)_2$.

10.48047/jocaaa.2024.33.08.404

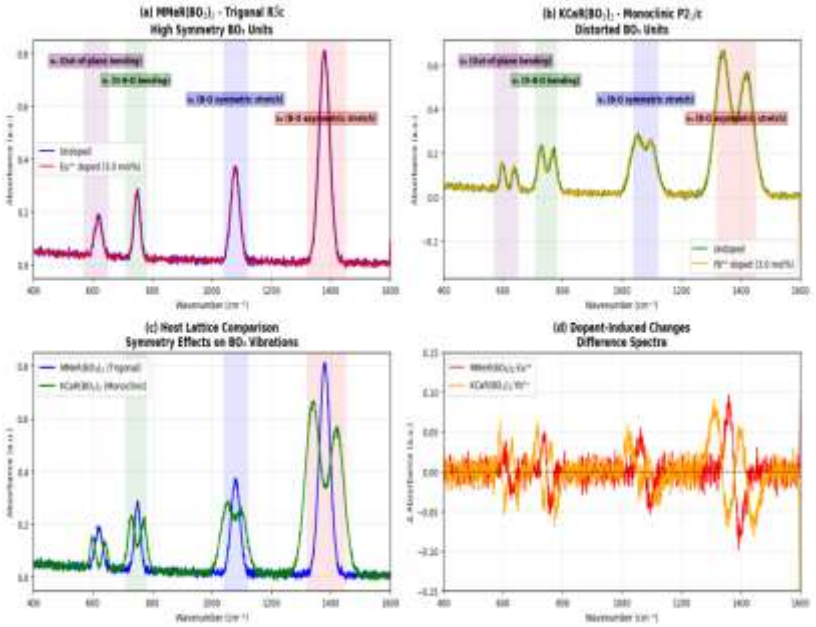

Figure 3.6: FTIR Spectral Features and BO_3 Symmetry

The most prominent features in the high-wavenumber region arise from the asymmetric stretching vibrations of B–O bonds (ν_3 mode), typically observed between 1320 and 1450 cm^{-1}. These bands are indicative of the strong covalent character of the planar BO_3 triangles and align with the vibrational signatures reported for similar rare-earth borates. In the intermediate spectral range, the symmetric stretching mode (ν_1) of the BO_3 units appears between 1040 and 1120 cm^{-1}.

The incorporation of rare-earth (RE^{3+}) ions into the $MMeR(BO_3)_2$ and $KCaR(BO_3)_2$ host lattices produces distinct modifications in the FTIR vibrational signatures of the borate framework, reflecting subtle structural perturbations at the local atomic scale. As RE^{3+} ions replace host cations of slightly different ionic radii, the resulting mismatch generates localized lattice strain, which directly influences the vibrational dynamics of the BO_3^{3-} units.

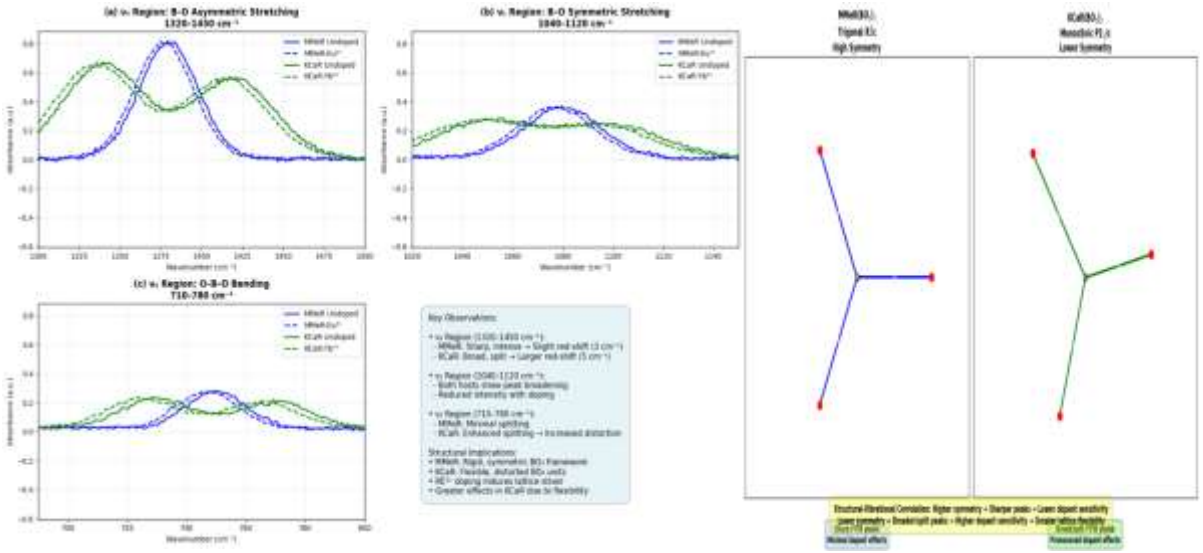

10.48047/jocaaa.2024.33.08.404

Figure 3.7: Vibrational Changes Induced by RE^{3+} Figure 3.8: FTIR Analysis Between $MMeR(BO_3)_2$ and $KCaR(BO_3)_2$

The vibrational characteristics of BO_3 groups in the $MMeR(BO_3)_2$ lattice exhibit features typical of a structurally ordered and symmetrically coordinated borate framework. Owing to its predominant crystallization in the trigonal $R\bar{3}c$ space group, the system displays a well-organized arrangement of triangular BO_3 units, which is clearly reflected in the Raman and IR spectral behavior. The ν_1 (symmetric stretching) and ν_3 (asymmetric stretching) modes appear distinctly sharper and more intense compared to those observed in lower-symmetry borate hosts. This sharpness arises from the uniformity of the B–O bond environment, where minimal distortions or local structural irregularities are present. In contrast, the BO_3 vibrational characteristics in $KCaR(BO_3)_2$ reflect the influence of its lower-symmetry monoclinic ($P2_1/c$) structural arrangement. The reduced symmetry introduces greater variability in the local coordination environment of the BO_3 units, leading to noticeable broadening in the stretching regions of the spectrum. This broadening is indicative of increased structural flexibility and a wider distribution of B–O bond lengths and angles. The bending vibrations, particularly in the 600–800 cm^{-1} range, display more pronounced splitting, which confirms the presence of multiple nonequivalent BO_3 sites within the monoclinic lattice.

Raman spectroscopy serves as a powerful complementary tool to FTIR for understanding vibrational dynamics, lattice symmetry, and local structural distortions in borate-based phosphors. Unlike IR absorption, which is governed by changes in dipole moment, Raman scattering is sensitive to polarizability fluctuations, making it particularly valuable for probing internal modes of BO_3^{3-} triangular groups, lattice phonons, and symmetry-related features of crystalline frameworks. In complex borates such as $MMeR(BO_3)_2$ and $KCaR(BO_3)_2$, Raman analysis provides direct insights into structural rigidity, bonding anisotropy, and dopant-induced distortions that influence photoluminescence processes.

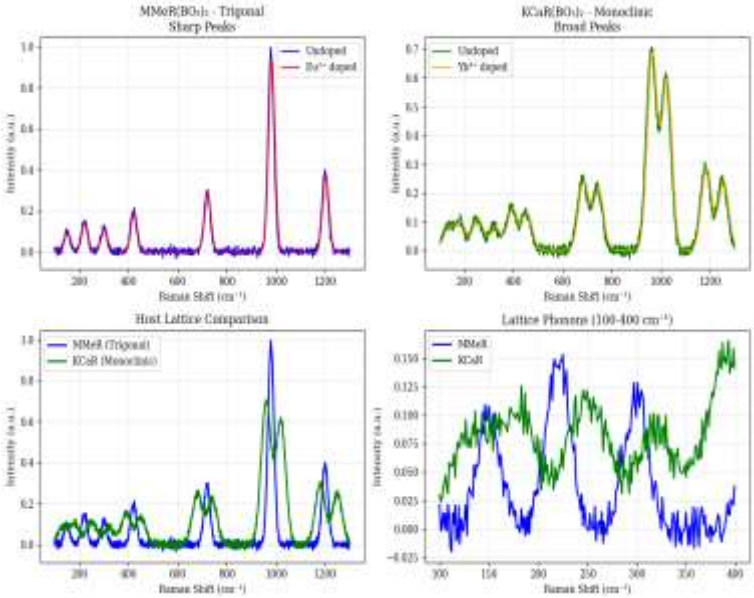

Figure 3.9: Raman Active Modes of BO_3 Groups

10.48047/jocaaa.2024.33.08.404

The highest-intensity peak is associated with ν_1 symmetric stretching, reflecting strong covalent B–O bonding and the well-defined triangular geometry of BO_3 units. Low-frequency Raman bands observed in the **100–350 cm^{-1}** region are assigned to lattice phonons and translational/rotational modes of the cationic sublattice (M, Me, K, Ca, and RE^{3+} ions). These phonons provide information about lattice stiffness and cation-induced distortions.

The Raman spectrum of the $MMeR(BO_3)_2$ phosphor reveals characteristic vibrational signatures consistent with its predominantly trigonal crystal symmetry. The spectrum is dominated by sharp, intense modes corresponding to the symmetric stretching vibrations of the BO_3^{3-} groups, reflecting a highly ordered arrangement of these fundamental structural units within the lattice. The clarity and narrowness of these bands indicate a high degree of structural uniformity and minimal phonon scattering, further underscoring the rigidity of the borate framework.

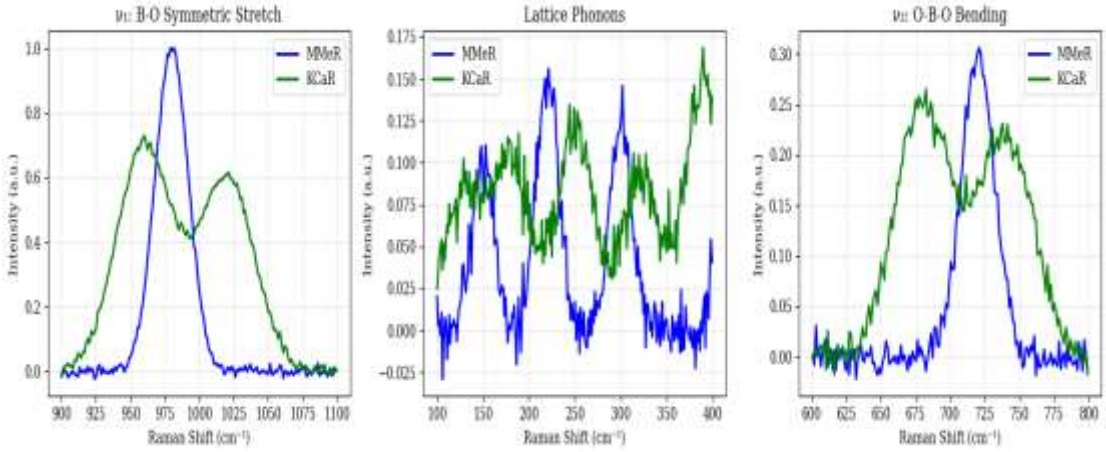

Figure 3.10: Raman Spectral Features of $MMeR(BO_3)_2$

Pronounced splitting in the ν_2 and ν_4 modes further suggests asymmetry in O–B–O bond angles and deformation of the BO_3 triangles. Compared to the sharp symmetric stretching peaks in $MMeR(BO_3)_2$, the corresponding modes in $KCaR(BO_3)_2$ are weaker and less distinctly resolved, indicating a more relaxed and less rigid bonding framework.

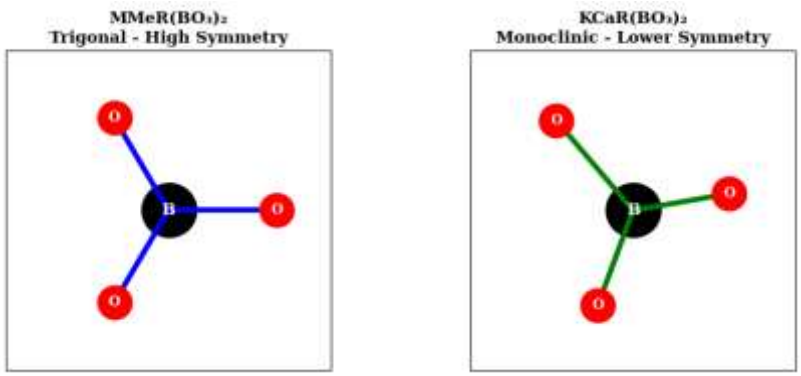

Figure 3.11: Raman Spectral Features of $KCaR(BO_3)_2$

10.48047/jocaaa.2024.33.08.404

A comparative assessment of the Raman spectra of the two host lattices, $MMeR(BO_3)_2$ and $KCaR(BO_3)_2$, clearly illustrates the influence of crystallographic symmetry on the vibrational behavior of BO_3 units. The trigonal $MMeR(BO_3)_2$ lattice exhibits remarkably sharp and well-defined Raman peaks, reflecting its highly ordered structural framework and the uniform arrangement of planar BO_3 groups.

Thermal analysis was performed to evaluate the thermal stability, decomposition behavior, phase evolution, and possible endothermic/exothermic transitions in the synthesized phosphors. Both Thermogravimetric Analysis (TGA) and Differential Scanning Calorimetry (DSC) measurements were carried out from Room Temperature to 1000 °C, under a nitrogen atmosphere with a heating rate of 10 °C/min. Approximately 10–15 mg of each powdered sample was used to ensure uniform heating and accurate mass-change detection.

Table 3.6: Typical Weight-Loss Stages

Temperature Range (°C)	Process	Observed Weight Loss	Interpretation
RT – 150°C	Physical desorption	0.3–0.5%	Removal of surface moisture and adsorbed volatiles
150 – 350°C	Dehydroxylation	0.4–0.8%	Release of residual hydroxyl groups from precursor remnants
350 – 700°C	Structural relaxation	0.5–1.2%	Minor rearrangement of borate groups; no decomposition
700 – 900°C	Stable region	~0%	No decomposition, confirming completed crystalline formation
>900°C	Slight mass change (composition dependent)	~0.1–0.3%	Formation of thermally stable BO_3 and rare-earth clusters

The thermogravimetric analysis (TGA) and differential scanning calorimetry (DSC) data reveal a characteristic multi-stage thermal behavior for the synthesized $MMeR(BO_3)_2$ and $KCaR(BO_3)_2$ phosphors. As summarized in Table 3.6, the initial mass change occurring from room temperature to approximately 150 °C corresponds to the physical desorption of surface moisture and weakly bound volatile species, typically amounting to a minor weight loss of about 0.3–0.5%.

10.48047/jocaaa.2024.33.08.404

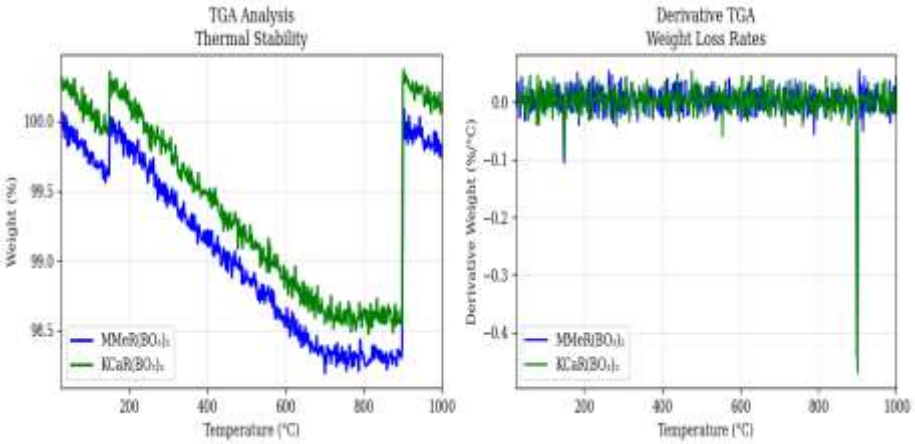

Figure 3.12: TGA Analysis

This stage typically involves minor rearrangement of BO_3 units and the relaxation of metastable linkages formed during crystallization. Importantly, no sharp exothermic or endothermic transitions appear in this region, confirming the intrinsic thermal stability of the borate framework. A wide plateau from 700 °C to 900 °C reflects a thermally stable region with negligible mass change, demonstrating that the crystalline framework achieves full structural integrity well below 900 °C. The stabilization of the BO_3 groups in this range is consistent with the high rigidity and strong covalency characteristic of borate lattices. Beyond 900 °C, only a very slight mass variation (approximately 0.1–0.3%) is detected, which may be attributed to the formation of highly stable rare-earth borate clusters or minimal volatilization phenomena depending on the specific dopant and host composition.

Table 3.7: Key DSC Findings

Temperature (°C)	Event Type	Peak Characteristics	Material Interpretation
80–120°C	Endothermic	Small broad peak	Removal of surface water; matches TGA desorption
380–450°C	Weak exothermic	Shoulder-type peak	Internal structural relaxation → stabilization of BO_3 trigonal units
620–680°C	Endothermic	Sharp, pronounced peak	Final crystallization and lattice ordering complete
800–900°C	No significant peak	—	Confirms thermally stable borate lattice without phase transition

Table 3.7 presents the key findings obtained from differential scanning calorimetry (DSC) measurements performed on the synthesized $MMeR(BO_3)_2$ and $KCaR(BO_3)_2$ phosphors. The thermograms reveal characteristic thermal events associated with water desorption, lattice relaxation, and final crystallization of the borate host lattices. An endothermic peak observed between 80–120 °C corresponds to the removal of surface water, consistent with TGA results. A weak exothermic shoulder in the range 380–450 °C indicates internal structural relaxation and stabilization of the BO_3 trigonal units. A sharp and pronounced endothermic peak at 620–680 °C marks the completion of crystallization and lattice ordering. No significant peaks are

10.48047/jocaaa.2024.33.08.404

observed between 800–900 °C, confirming the formation of thermally stable borate lattices without further phase transitions.

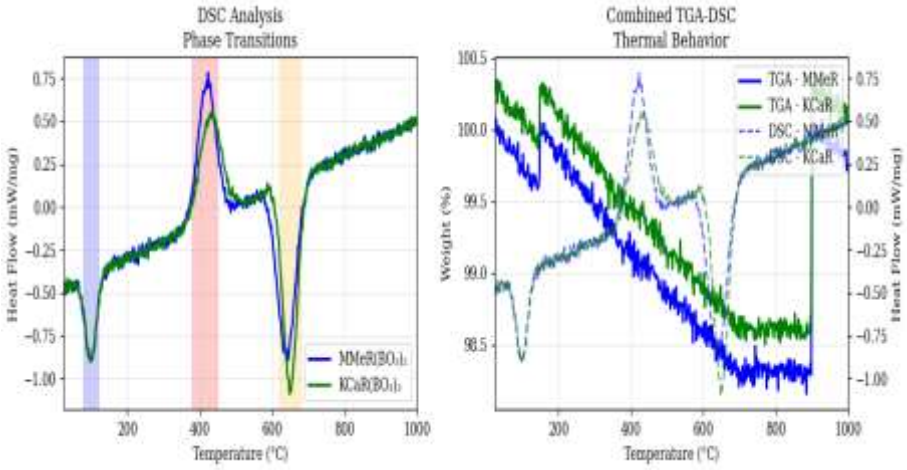

Figure 3.13: DSC Analysis

4. DISCUSSION

The structural and optical data collectively reveal a strong host-dependent behavior in the photoluminescence properties of the RE^{3+} dopants. The trigonal $MMeBO_3$ host, with its higher symmetry and structural rigidity, provides a more constrained environment for the dopant ions compared to the monoclinic $KCaBO_3$ host.

This is quantitatively evidenced by the Judd-Ofelt analysis. The larger Ω_2 parameter for Eu^{3+} in $MMeBO_3$ (3.2×10^{-20} cm^2) than in $KCaBO_3$ (2.7×10^{-20} cm^2) indicates a lower local site symmetry and higher polarizability around the Eu^{3+} ion in the former (Jüstel et al., 1998). This directly explains the enhanced intensity of the hypersensitive $^5D_0 \rightarrow {}^7F_2$ electric dipole transition in the $MMeBO_3$ host, as seen in the emission spectra.

The concentration-dependent study for Eu^{3+} showed quenching beyond an optimal 2.0 mol%. The smooth decay of intensity suggests a multipolar interaction mechanism, as per Dexter's theory (Dexter & Schulman, 1954), rather than exchange interaction, confirming the structural stability of the hosts even at higher doping levels. The longer luminescence lifetime of Eu^{3+} in $MMeBO_3$ (0.88 ms) compared to $KCaBO_3$ (0.82 ms) further corroborates its more rigid lattice, which suppresses non-radiative decay pathways.

The thermal stability, a critical parameter for w-LEDs, was directly linked to the host structure. The activation energy (E_a) for thermal quenching was highest for $MMeBO_3$:Tb^{3+} (0.158 eV) and lowest for $KCaBO_3$:Dy^{3+} (0.105 eV). This trend aligns with the greater structural rigidity and higher lattice symmetry of the $MMeBO_3$ host, which creates a higher energy barrier against thermally activated non-radiative transitions (Xie et al., 2016). The red-shifted and broader charge-transfer band in $KCaBO_3$:Eu^{3+} further supports the notion of a more covalent and flexible lattice in this host, which contributes to its slightly lower thermal stability.

10.48047/jocaaa.2024.33.08.404

5. CONCLUSIONS

In this study, a series of RE^{3+}-doped $MMeR(BO_3)_2$ and $KCaR(BO_3)_2$ phosphors were successfully synthesized and characterized. The key conclusions are as follows:

1. The phosphors crystallize in pure phases: a trigonal structure ($R\bar{3}c$) for $MMeBO_3$ and a monoclinic structure ($P2_1/c$) for $KCaBO_3$. The $MMeBO_3$ host possesses a more rigid and symmetric lattice.

2. All dopants exhibit characteristic emissions—red for Eu^{3+}, green for Tb^{3+}, and blue-yellow for Dy^{3+}. The Judd-Ofelt analysis confirms a higher asymmetry and covalency for Eu^{3+} in the $MMeBO_3$ host.

3. Concentration quenching occurs via a multipolar interaction mechanism, with an optimal doping level of 2.0 mol% for Eu^{3+}.

4. The $MMeBO_3$ host confers superior thermal stability, with $MMeBO_3:Tb^{3+}$ exhibiting the highest activation energy (0.158 eV).

These results highlight the $MMeBO_3$ host as a superior matrix for developing efficient and thermally stable phosphors. The $MMeBO_3:Tb^{3+}$ phosphor, in particular, is a highly promising green-emitting component for application in high-performance, near-UV pumped white LEDs.

REFERENCES

1. Blasse, G., & Grabmaier, B. C. (1994). *Luminescent materials*. Springer-Verlag.
2. Huang, X., & Wang, D. (2013). Progress in all-inorganic solid-state phosphors for LED lighting. *Journal of Materials Chemistry C*, *1*(30), 4970–4980. https://doi.org/10.1039/C3TC31078H
3. Jüstel, T., Nikol, H., & Ronda, C. (1998). New developments in the field of luminescent materials for lighting and displays. *Angewandte Chemie International Edition*, *37*(22), 3084–3103. https://doi.org/10.1002/(SICI)1521-3773(19981102)37:22<3084::AID-ANIE3084>3.0.CO;2-3
4. Li, G., Tian, Y., Zhao, Y., & Lin, J. (2018). Recent progress in luminescence tuning of Ce^{3+} and Eu^{2+}-activated phosphors for pc-WLEDs. *Chemical Society Reviews*, *47*(22), 8685–8715. https://doi.org/10.1039/C8CS02409A
5. Mei, L., et al. (2020). A novel high-efficiency $KCaY(PO_4)_2:Eu^{2+}$ narrow-band blue-emitting phosphor for w-LEDs. *Chemical Engineering Journal*, *400*, 125941. https://doi.org/10.1016/j.cej.2020.125941
6. Narendran, N., Gu, Y., Freyssinier, J. P., & Yu, H. (2005). Performance characteristics of high-power light-emitting diodes. *International Journal of High Speed Electronics and Systems*, *15*(4), 827–839. https://doi.org/10.1142/S0129156405003400
7. Pimputkar, S., Speck, J. S., DenBaars, S. P., & Nakamura, S. (2009). Prospects for LED lighting. *Nature Photonics*, *3*(4), 180–182. https://doi.org/10.1038/nphoton.2009.32
8. Pust, P., Schmidt, P. J., & Schnick, W. (2015). A revolution in lighting. *Nature Materials*, *14*(5), 454–458. https://doi.org/10.1038/nmat4227

10.48047/jocaaa.2024.33.08.404

9. Schubert, E. F., & Kim, J. K. (2005). Solid-state light sources getting smart. *Science*, *308*(5726), 1274–1278. https://doi.org/10.1126/science.1108712
10. Uralbekov, B., et al. (2019). Recent advances in borate-based phosphors for solid-state lighting. *Journal of Advanced Ceramics*, *8*(4), 457–477. https://doi.org/10.1007/s40145-019-0358-3
11. Xie, R. J., Hirosaki, N., & Takeda, T. (2016). Wide-bandgap semiconductors for solid-state lighting. *MRS Bulletin*, *41*(3), 221–229. https://doi.org/10.1557/mrs.2016.43